Modulating Coordination Environment of Cobalt-Based Spinel Octahedral Metal Sites to Boost Metal−Oxygen Bond Covalency for Reversible Lithium−Oxygen Batteries

Yu Pan[a, #], *Anjun Hu*[a,#,*], *Ruizhe Xu*[a,#], *Jingze Chen*[a], *Borui Yang*[a], *Ting Li*[a], *Kun Li*[a], *Yuanjian Li*[b], *Zhi Wei Seh*[b,*], *Jianping Long*[a,*]

[a] College of Materials and Chemistry & Chemical Engineering, Chengdu University of Technology, 1#, Dongsanlu, Erxianqiao, Chengdu 610059, Sichuan, P. R. China

[b] Institute of Materials Research and Engineering (IMRE), Agency for Science, Technology and Research (A*STAR), 2 Fusionopolis Way, Innovis #08-03, Singapore 138634, Republic of Singapore

* Corresponding author: anjunhu@cdut.edu.cn (Anjun Hu); sehzw@imre.a-star.edu.sg (Zhi Wei Seh); longjianping@cdut.cn (Jianping Long)

[#] These authors contributed to this work equally.

ABSTRACT: The intrinsic catalytic activity of conventional spinel electrocatalysts hinders their electrocatalytic outcomes in lithium−oxygen batteries (LOBs), despite their appeal due to compositional variety and structural adaptability. In this work, we reveal that the electrocatalytic activities of these catalysts can be inherently enhanced by modulating metal−oxygen (M−O) bond covalency interactions through the introduction of the Cr element into the $MnCo_2O_4$ octahedral sites ($MnCr_{0.5}Co_{1.5}O_4$). The introduction of Cr^{3+} directly alters the coordination structure of Co octahedral sites, which increases the Co^{3+}−O distance and reduces the lattice symmetry, resulting in an enhanced covalency interactions of M−O bond. Computational analysis supports the effectiveness of Cr in altering the electronic structure of the active site, narrowing the energy gap between Co 3d and O 2p orbitals, evidencing the enhancement of the M−O covalency. In addition, this increased M−O covalency accelerates charge transfer in oxygen-related reactions, thereby contributing to the deposition and decomposition kinetics of discharge products in LOBs. As a proof of concept, the $MnCr_{0.5}Co_{1.5}O_4$ catalyzed LOBs exhibit a large discharge capacity of 16388.3 mAh g^{-1} and maintain stability over 329 cycles. This work paves the way for the development of reversible LOBs by manipulating the coordination structure of spinel catalysts.

KEYWORDS: *Spinel electrocatalysts; Metal−oxygen covalency; Coordination Environment; Li_2O_2 nucleation site; Lithium−oxygen batteries*

Lithium−oxygen batteries (LOBs) have garnered significant attention in the field of electrochemical energy storage and conversion due to their high theoretical specific energy of 3500 Wh kg^{-1} and environmentally friendly nature[1–4]. However, the commercialization of LOBs still presents substantial challenges primarily because their discharge process ($2Li^+ + 2e^- + O_2 \leftrightarrow Li_2O_2$ (2.96 V *vs.* Li/Li^+)) involves the formation and decomposition of insulation insoluble discharge products[5–7]. The incomplete decomposition and accumulation of Li_2O_2 during cycling result in reduced capacity, increased overpotentials, cycling instability, and inferior rate performance of the battery[8,9]. Therefore, developing a stable and cost-effective cathode catalyst with high catalytic activity for oxygen reduction (ORR) and oxygen evolution reaction (OER) is crucial for improving the electrochemical performance of LOBs.

Spinel oxides have been identified as promising candidates for high-efficiency electrocatalysts in recent studies due to their unique tunable coordination structure and diverse constituent elements, which allow for easy regulation of their active site electrocatalytic activity[10–12]. Specifically, the octahedral sites within spinel oxides are known to play a crucial role in adsorbing various reaction intermediates ($*O_2$, $*LiO_2$, and $*Li_2O_2$) and facilitating the efficient conversion and integration of adjacent intermediates during the OER/ORR reaction process, thereby significantly enhancing the reaction kinetics of LOBs[12–14]. Despite these advantages, pristine spinel catalysts often exhibit an upper limit to the catalytic activity of their octahedral sites, posing challenges in achieving optimal catalytic effects in subsequent electrocatalytic reactions. Therefore, the rational adjustment of the spinel coordination structure to optimize the electronic structure of the octahedral sites is crucial for obtaining electrocatalysts with enhanced catalytic activity.

In spinel, both covalent and ionic interactions occur between metal (narrow d band) and oxygen (broad p band), which typically influence the interactions between the metal active site and oxygen-

containing intermediates[15–17]. It is suggested that modulation of metal−oxygen (M−O) covalency plays a key role in enhancing catalytic activity and speeding up reaction kinetics. Strengthening the M−O covalency can lead to several beneficial effects. Firstly, it can decrease the energy gap between the oxygen 2p band center and the metal 3d band center[18–20], facilitating more flexible electronic interactions. Additionally, this modification alters the electronic structure of the metal active site, optimizing the electrocatalytic activity to adjust the adsorption energy of intermediate products. Consequently, this adjustment ultimately reduces the reaction barrier and accelerates the OER/ORR reaction kinetics. For example, Wang et al. demonstrated that exposing abundant active sites through in situ Al leaching increased the M−O covalency, significantly lowering the oxidation activation energy and potential barrier for electrical transfer at the Fe/Co/Ni sites[18]. Similarly, Lv et al. successfully enhanced nickel-oxygen (Ni−O) covalency in conductive high-valence nickel catecholate framework (Ni^{III}-NCF) nanowire arrays by spin-state modulation, which improved electron exchange between Ni^{III}-NCF and oxygen-containing intermediates, accelerating the ORR reaction kinetics[20]. Moreover, influencing the coordination structure of spinel oxides through cationic substitution allows for electron redistribution, optimizing the electronic structure of the active site to strengthen the M−O covalency, thereby enhancing ORR/OER electrocatalytic activity. Therefore, the direct modification of the coordination environment of spinel octahedral metal sites to enhance the M−O covalency can effectively accelerate the OER/ORR reaction kinetics and enhance the electrochemical performance of LOBs.

In this study, a spinel electrocatalyst Cr_2-$MnCo_2O_4$ ($MnCr_{0.5}Co_{1.5}O_4$) was meticulously synthesized using the hydrothermal method to explore the impact of M−O covalency enhancement on the electrochemical performance of LOBs by incorporating Cr into the octahedral sites of $MnCo_2O_4$. The introduction of Co^{3+} into $MnCo_2O_4$ results in an elongation of the Co^{3+}−O bond distance and a

reduction in lattice symmetry, causing a notable alteration in the coordination structure of the Co octahedral sites. This leads to a rearrangement of electrons, directly optimizing the M-O covalency of the catalytic active sites and thus enhances the electrocatalysis. Density functional theory calculations (DFT) have confirmed that the presence of Co^{3+} enhances the Co−O covalency in the $MnCo_2O_4$ spinel, facilitating electronic interactions and significantly accelerating the kinetics of OER/ORR. Furthermore, the introduction of Co^{3+} optimizes the electronic structure of the Co site, with the d-band center shifting toward the Fermi energy level. This adjustment enhances the adsorption of reaction intermediates on the cathode surface, promoting the reversible formation and decomposition of Li_2O_2. Consequently, the Cr_2-$MnCo_2O_4$-based LOBs demonstrate a relatively high specific discharge capacity of 16388.3 mAh g^{-1} and an extended cycle life of 329 cycles, far superior to that of the pristine spinel $MnCo_2O_4$ based LOBs.

RESULTS AND DISCUSSION

DFT calculations were first conducted to assess the electrocatalytic activity of spinel electrocatalysts for ORR/OER reactions[14,21,22]. At the Fermi energy level (E_f), Cr_2-$MnCo_2O_4$ exhibits a high total density of states (TDOS), suggesting the presence of free electrons (**Figures** 1a and **Figures** S1)[23–25]. The band gap of Cr_2-$MnCo_2O_4$ is notably lower compared to the other samples, indicating enhanced electrical conductivity, which is advantageous for charge transfer. Subsequently, the projected density of states (PDOS) of Co and O in the three samples was further examined in **Figures** 1b-1d. It was observed that with the introduction of Cr, the coordination structure of the Co octahedron changes, resulting in an increase in active electrons at the Co site. This change favors the hybridization between the Co 3d and O 2p orbitals, thereby facilitating electrochemical reactions. Furthermore, the quantification of metal−oxygen (M−O) covalency was determined by the distance denoted as charge-transfer energy (Δ), in units of electron volts (eV), between the metal 3d band center and O 2p band

center of the three samples (**Figure** S2)[16,26,27]. Based on this analysis, the charge transfer energies of the Co 3d band center and O 2p band center of the three samples were calculated. It was observed in **Figure** 1d that Cr_2-$MnCo_2O_4$ exhibited the smallest charge transfer energy (Δ= 0.520 eV), as compared to $MnCo_2O_4$ (Δ= 1.368 eV) and Cr_1-$MnCo_2O_4$ (Δ= 0.667 eV), indicating a stronger M−O covalency. This stronger covalency leads to enhanced electronic interactions between Co sites and neighboring O sites. Notably, the Co d-band center of Cr_2-$MnCo_2O_4$ was found to be closer to the E_f, causing a reduction in electron occupation of the corresponding antibonding orbitals in comparison to the other two samples. This reduction enhances its adsorption capacity for reaction intermediates, thereby effectively promoting the reversible formation and decomposition of discharge products. Consequently, the optimization of Co 3d orbitals and the reinforcement of M−O covalency in Cr_2-$MnCo_2O_4$ are anticipated to improve the electrocatalytic performance of Co-based spinel.

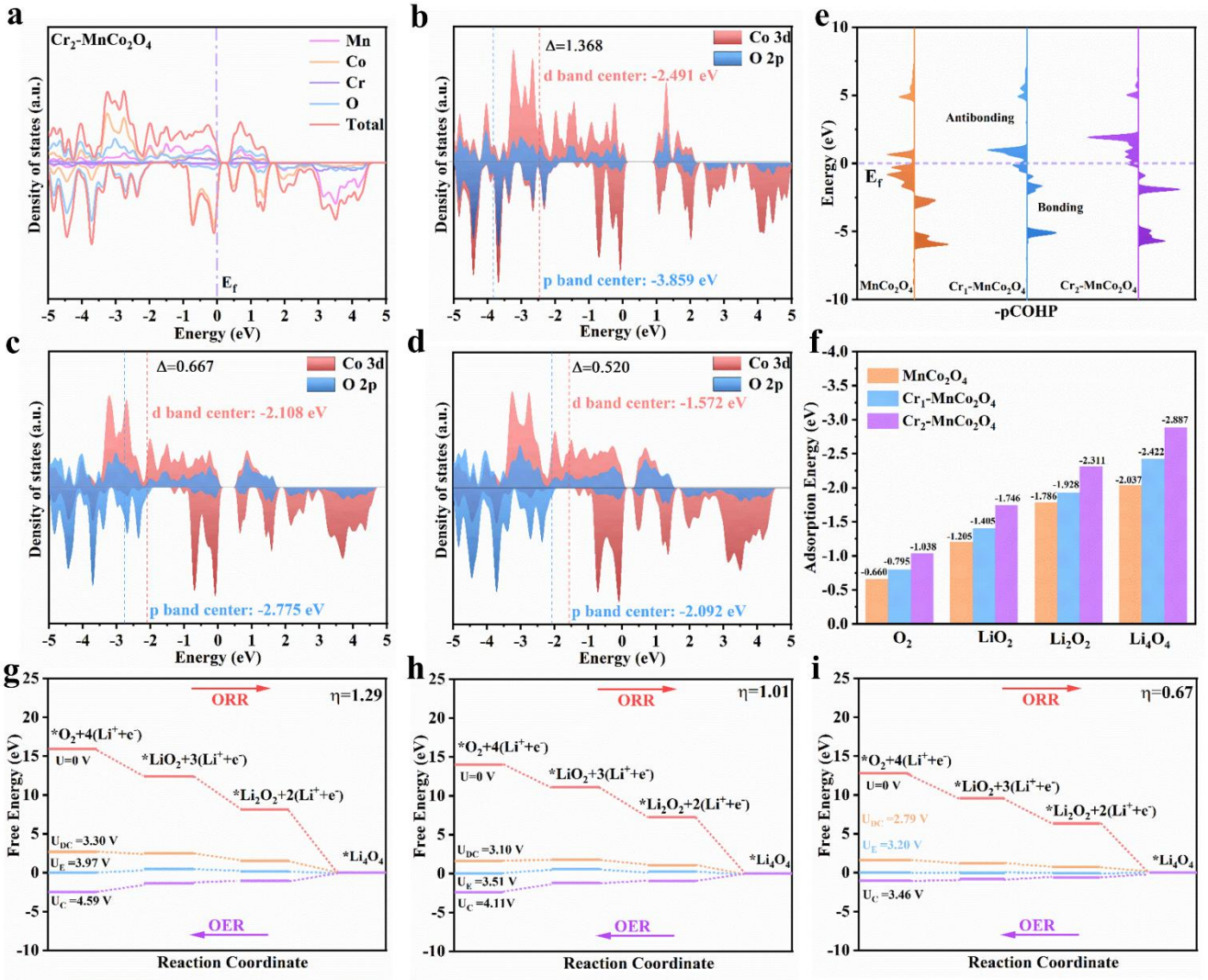

Figure 1. Total DOS of (a) Cr_2-$MnCo_2O_4$. PDOS of Co 3d orbital and O 2p orbital for (b) $MnCo_2O_4$ (c) Cr_1-$MnCo_2O_4$ and (d) Cr_2-$MnCo_2O_4$. (e) COHP analysis of the Co−O bond on three samples. (f) The adsorption energy of three samples towards different reaction intermediates. Free energy diagrams for (g) $MnCo_2O_4$ (h) Cr_1-$MnCo_2O_4$ and (i) Cr_2-$MnCo_2O_4$.

With the purpose of exploring the effect of the optimized Co active site on the adsorption of oxygen-containing intermediates, an analysis of the PDOS of three samples with adsorbed intermediates was then carried out. As shown in the **Figures** S3-S5, it can be clearly seen that the catalytic active site Co 3d orbital overlaps with the DOS of the O 2p orbital of the reaction intermediate, indicating the formation of Co−O bonds. The overlap of between the 3d orbitals and O 2p orbitals in Cr_2-$MnCo_2O_4$ is notably larger than that in $MnCo_2O_4$, indicating enhanced Co−O bonding ability and thereby facilitating the acceleration of the electrocatalytic reaction. Moreover, bonding interactions between Co active sites and reaction intermediates were examined using the

crystal orbital Hamilton population (COHP) method, where negative COHP (right) indicates bonding contribution and positive COHP (left) indicate antibonding contribution. The dominance of the intensity of the Co−O bond by incompletely occupied antibonding orbitals located below the Fermi level allows for a complete occupation of all bonding orbitals (**Figure 1**e)[28–30]. The antibonding orbitals of Cr_2-$MnCo_2O_4$ are notably well above the E_f, with correspondingly low occupancy levels, indicating robust orbital interactions between the Co site and oxygen-containing intermediates. To further assess the Co−O bonding capacity, the integrated crystal orbital Hamilton populations (ICOHP) were calculated (**Table** S1), revealing that Cr_2-$MnCo_2O_4$ exhibits a smaller ICOHP value (−3.166) compared to $MnCo_2O_4$ (−2.115) and Cr_1-$MnCo_2O_4$ (−2.915). This tangible difference demonstrates the superior Co−O binding ability of Cr_2-$MnCo_2O_4$. The optimized Co active site's enhanced ability to bind reaction intermediates fosters stronger electronic interactions between them, thereby expediting the reaction kinetics in OER/ORR processes.

The adsorption energy of the catalyst surface towards different stages of reaction intermediates is a crucial indicator for evaluating the electrochemical performance of LOBs, which is closely related to the reversible formation and decomposition of the discharge products[31,32]. Optimized structural models were developed for three samples with varying reaction intermediates adsorbed as depicted **Figure** S6. Subsequent calculations were conducted to determine the adsorption energies of these samples for different oxygen-containing intermediates (**Figure 1**f). Among these, Cr_2-$MnCo_2O_4$ exhibited higher adsorption capabilities compared to that of $MnCo_2O_4$ and Cr_1-$MnCo_2O_4$ for the reaction intermediates O_2 (−1.038 eV), LiO_2 (−1.746 eV), Li_2O_2 (−2.311 eV), and Li_4O_4 (−2.887 eV). Notably, the growth of discharge products on the cathode surface in LOBs intricately linked to the adsorption performance[8,33]. Accordingly, in contrast to $MnCo_2O_4$ and Cr_1-$MnCo_2O_4$, the strong adsorption of Cr_2-$MnCo_2O_4$ promotes the increase of Li_2O_2 nucleation sites, thereby facilitating the

uniform growth of Li_2O_2 on the electrode surface. The discharge products generated are typically in close with the cathode surfaces, displaying a strong charge transfer capacity that optimizes the electrocatalytic reaction, thus facilitating the reversible formation and decomposition of Li_2O_2/LiO_2. Consequently, the advanced spinel catalysts can modulate the adsorption behavior of the reaction intermediates, thereby regulating the nucleation and growth processes of discharge products for the electrochemical reaction of LOBs.

The corresponding Gibbs free energies were calculated for each reaction stage during the formation of discharge products in LOBs[25,34,35]. **Figures** 1g-1i illustrates the corresponding Gibbs free energies for each reaction stage in the formation of the discharge products. Overpotential, defined as $\eta=U_C-U_{DC}$, where U_C is the minimum charge potential, U_{DC} denotes the maximum discharge potential and U_E represents the equilibrium potential, serves as the primary parameter for measuring the electrocatalytic activity of the cathode catalyst. The calculated overpotential of Cr_2-$MnCo_2O_4$ (η = 0.67 V) is lower than that of $MnCo_2O_4$ (η=1.29 V) and Cr_1-$MnCo_2O_4$ (η=1.01 V), indicating that it exhibits the optimal ORR/OER performance, as consistent with prior computational findings.

As illustrated in the **Figure** 2a, Cr^{3+} was firstly introduced controllably by quantitatively adjusting the Mn: Cr composition ratio in the precursor solution during hydrothermal treatment. Then the obtained precursor was subjected to high-temperature calcination treatment, which successfully obtained the Cr_2-$MnCo_2O_4$ electrocatalysts. X-ray diffractometer (XRD) analysis confirmed the successful preparation of all three samples, aligning with standard PDF cards (JCPDS No. 01-1130) (**Figure** S7). Moreover, with the continuous doping of Cr^{3+}, the characteristic peaks are slightly shifted to the left and the lattice expands, which is caused by the introduction of larger ionic radius of Cr^{3+} replacing the octahedral Co^{3+} sites. Inductively coupled plasma optical emission spectroscopy (ICP-OES) reveal that the Cr: Co molar ratios in Cr_1-$MnCo_2O_4$ and Cr_2-$MnCo_2O_4$ as 15:85 and 25:75,

respectively (**Table** S2), which effectively prove the controlled introduction of Cr^{3+}[36–38]. The scanning electron microscope (SEM) images (**Figure** 2b and **Figures** S8-S9) displayed a cubic, nanosheet-stacked morphology for all samples, with rougher surfaces upon Cr^{3+} addition, enhancing reaction intermediate adsorption and active site exposure. Additionally, the energy dispersive spectrometer elemental (EDS) mapping of Cr_2-$MnCo_2O_4$ (**Figures** 2c-g) shows uniform distribution of Cr, Mn, Co and O elements in the Cr_2-$MnCo_2O_4$, further validating Cr^{3+} incorporation.

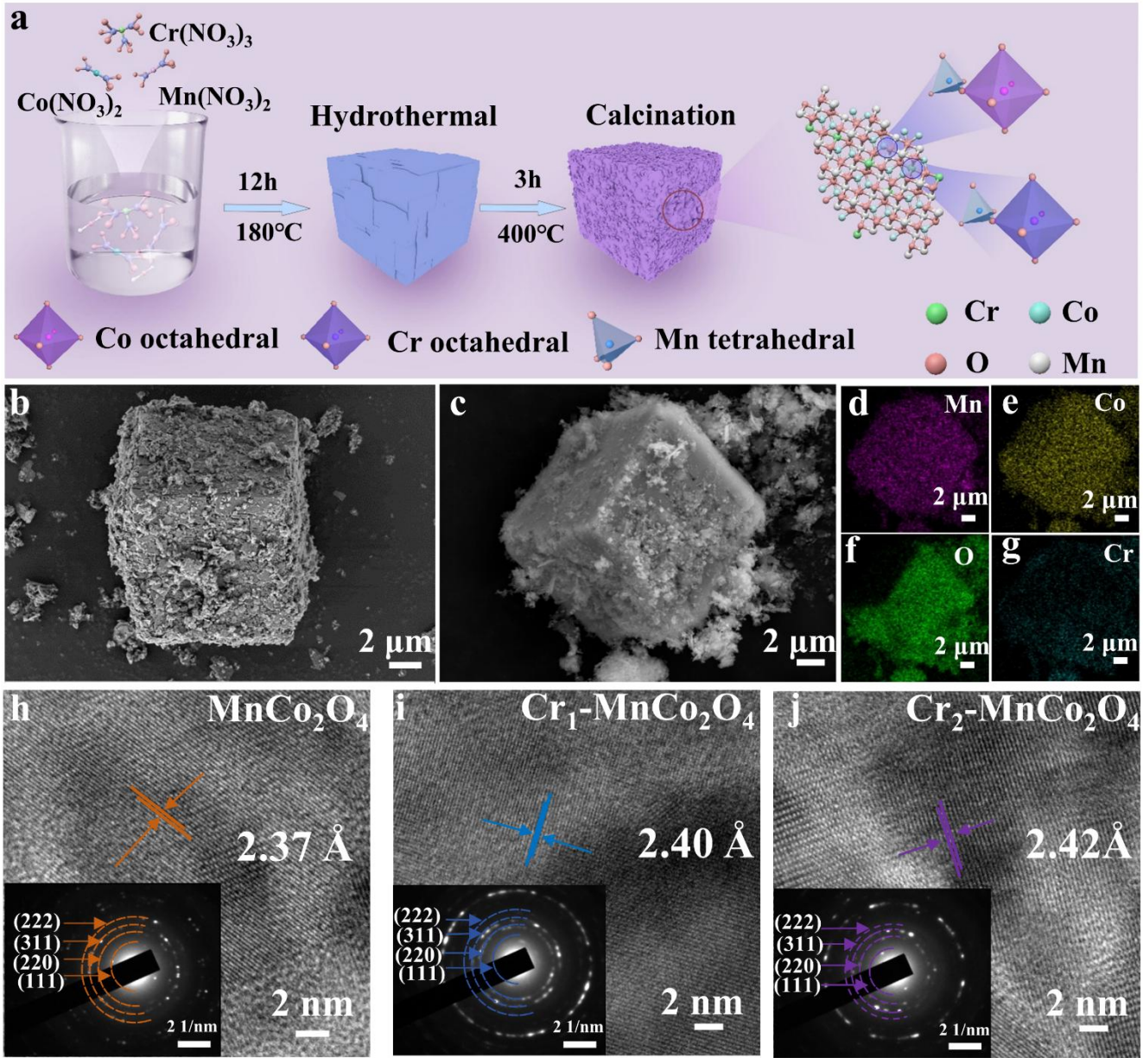

Figure 2. (a) Schematic illustration of the synthesis of the Cr_2-$MnCo_2O_4$ electrocatalysts. (b) SEM pattern of Cr_2-$MnCo_2O_4$. (c-g) EDS elemental mapping of Cr_2-$MnCo_2O_4$ (h-j) high-resolution TEM pattern and SAED pattern for $MnCo_2O_4$, Cr_1-$MnCo_2O_4$ and Cr_2-$MnCo_2O_4$.

Three samples were observed by high-resolution transmission electron microscopy (HR-TEM) to determine the effect of the introduction of Cr^{3+} on the crystal phase structure of $MnCo_2O_4$ (**Figures 2**h-j). It is evident from the observations that the lattice spacing on the (222) crystal plane of $MnCo_2O_4$ increases with the continuous introduction of Cr^{3+}. This increase is attributed to the lattice distortion resulting from the expansion of the octahedral coordination structure, aligning well with the XRD results. The selected-area electron diffraction (SAED) pattern of the three samples reveals multiple clear diffraction rings, indicating that the crystal structure of $MnCo_2O_4$ is not disrupted by the moderate introduction of Cr^{3+}. The relationship between the specific surface area of the catalyst, its pore size, and catalytic activity is crucial. The nitrogen adsorption and desorption isotherms of the three samples exhibit type IV isothermal curves with evident hysteresis lines (**Figure** S10)[39,40]. The pore size distribution curve shows that with the introduction of Cr, the pore size of the sample tends to increase. Comparing the specific surface areas of the samples (Table S3), it is found that Cr_2-$MnCo_2O_4$ has the largest specific surface area (115.81 $m^2\ g^{-1}$) among the three samples, with $MnCo_2O_4$ having 76.88 $m^2\ g^{-1}$ and Cr_1-$MnCo_2O_4$ having 89.14 $m^2\ g^{-1}$. This suggests that Cr_2-$MnCo_2O_4$ offers a larger area of catalytic activity. In summary, the Cr_2-$MnCo_2O_4$ samples exhibit rich mesoporous structures, exposing more catalytically active sites. This feature facilitates ion transport as well as the adsorption and storage of discharge products, enhancing the overall catalytic performance of the material.

To verify the effect of Cr^{3+} introduction on the coordination structure of $MnCo_2O_4$, Raman analyses were carried out on three samples[41–43]. In the **Figure** 3a, the presence of five distinct characteristic peaks can be clearly seen, which represent the F_{2g}, E_g, F_{2g}, F_{2g} and A_{1g} peaks. Notably, the A_{1g} peak at 692 cm^{-1} corresponds to the stretching vibration of the Co−O bond in the CoO_6 octahedron. To this end, the red shift of the A_{1g} peak in Cr_2-$MnCo_2O_4$ reflects a decrease in the

stretching frequency of the Co−O bonds in the octahedra, which increases the bond lengths, successfully changing the coordination structure of the Co octahedra. In addition, the relative content of oxygen vacancies inside the three samples was characterized by electron paramagnetic resonance (EPR) testing[20,44,45] (**Figure** 3b). At g = 2.0056, the plots of three samples all produced obvious signals, indicating the presence of oxygen vacancies. Apparently, Cr_2-$MnCo_2O_4$ exhibits the strongest signal, which indicates a higher concentration of oxygen vacancies and implying a modification in the coordination environment.

Changes in the coordination structure of spinel electrocatalysts are accompanied by changes in the corresponding electronic structure. X-ray photoelectron spectroscopy (XPS) was utilized to confirm these electronic structure changes in the three samples[46–50]. As shown in **Figure** 3c, the Co 2p spectrum of $MnCo_2O_4$ appeared two spin-orbit peaks (Co $2p_{1/2}$ and Co $2p_{3/2}$) were observed through deconvolution. These peaks corresponded to Co^{3+} (780.0 and 795.2 eV) and Co^{2+} (781.2 and 796.3 eV) peaks were present, respectively. Likewise, in **Figure** 3d, the Cr 2p spectrum display Cr $2p_{1/2}$ and Cr $2p_{3/2}$ spin-orbit peaks, where Cr^{2+} (575.4 and 584.7 eV), Cr^{3+} (576.6 and 586.0 eV), and Cr^{6+} (578.5 and 587.8 eV) peaks exist, respectively. Following the introduction of Cr^{3+}, Co loses electrons and the corresponding orbital peaks move to higher binding energies, whereas Cr gains electrons and the corresponding orbital peaks move to lower binding energies, which fully demonstrates that the octahedral coordination structure change induces the electronic rearrangement of the Co site. Furthermore, for the Mn 2p spectrum (**Figure** S11a), the positions of the corresponding orbital peaks before and after the reaction show no significant change without affecting the subsequent reaction. In O 1s spectrum (**Figure** S11b), the binding energy of O 1s is positively shifted, indicating that the O electronic structure is also optimized.

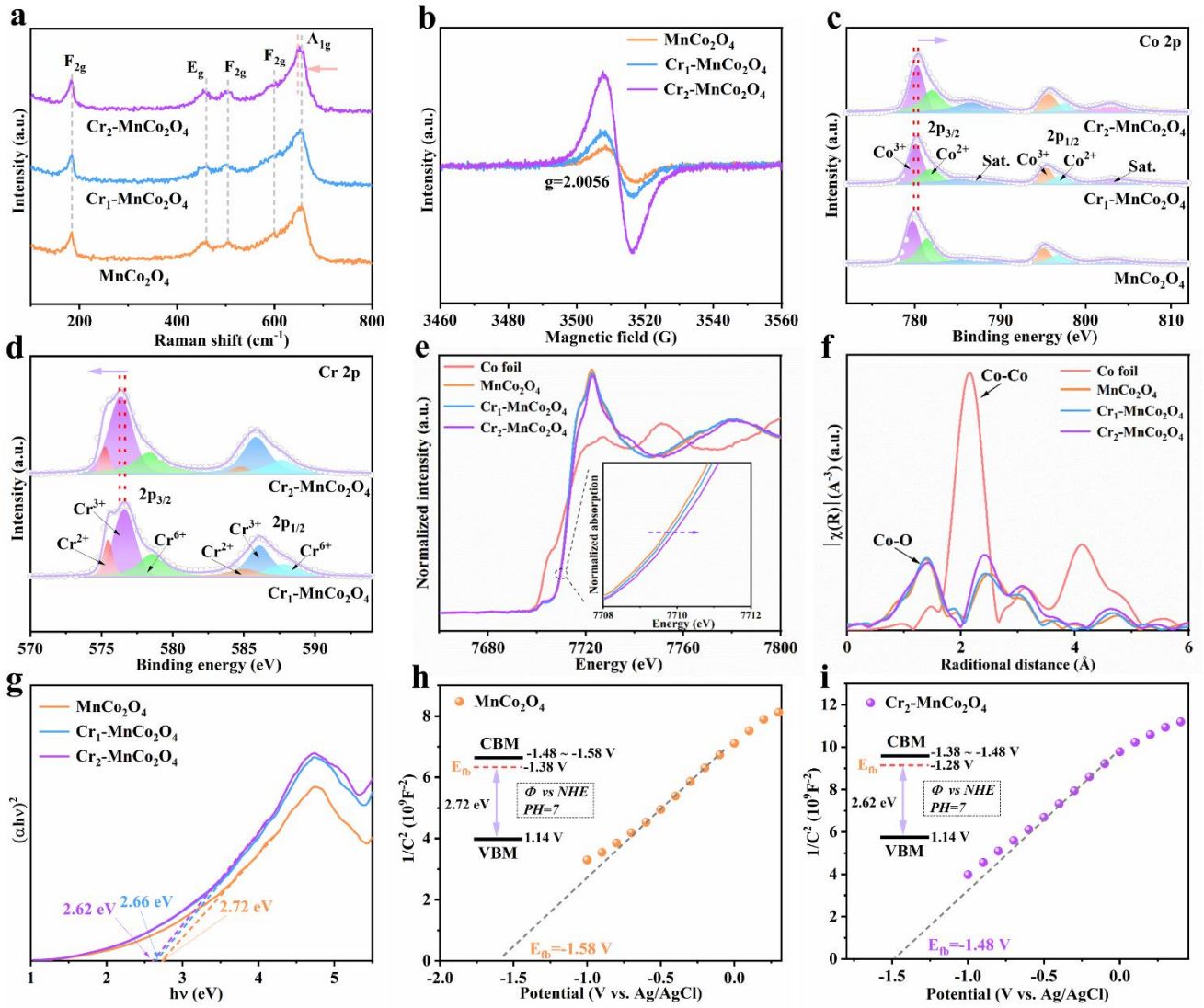

Figure 3. Structural characterization for $MnCo_2O_4$, Cr_1-$MnCo_2O_4$ and Cr_2-$MnCo_2O_4$. (a) Raman spectrum for three samples. (b) EPR spectrum for three samples. (c-d) Co 2p and Cr 2p high-resolution XPS spectra for as-prepared samples. (d) Hysteresis loops of three samples recorded at room temperature (300 K). (e) Normalized K-edge XANES for three samples and Co foil. (f) K-edge FT-EXAFS in R space for three samples and Co foil. (g) UV diffuse reflectance spectrum of three samples by K-M transformation. (h) Mott-Schottky plots of electrodes containing $MnCo_2O_4$ and calculated redox potentials. (i) Mott-Schottky plots and calculated redox potentials for electrodes containing Cr_2-$MnCo_2O_4$.

K-edge X-ray absorption near edge structure (XANES) and extended X-ray absorption fine structure (EXAFS) analyses were carried out for further determination of the valence and partial coordination environments of the Co active sites in the electrocatalysts[10,47,51,52]. As demonstrated in **Figure** 3e, with the introduction of Cr^{3+}, the absorption edges of the Co K-edges XANES move to higher energy levels. This shift signifies the increasing valence states, consistent with the XPS

results[50,53,54]. Particularly, it can be clearly seen that Cr_2-$MnCo_2O_4$ has the highest valence state, which reveals an efficient transfer of electrons from Co to neighboring O. This transfer inevitably triggers a charge off-domain around the Co active site. In addition, the intensity of the white line peak in Cr_2-$MnCo_2O_4$ is slightly smaller than that of the other samples, which indicates that the disordered arrangement of the active site, thus resulting in the enhancement of the electron density within the Co 3d orbitals[10], in line with the prediction of theoretical calculations. As shown in **Figure** 3f, the first peak of the Co K-edge R-space spectrum located around 1.5 Å is assigned to the single scattering path of the metal ion to the neighboring oxygen, which is Co−O bond, and the adjacent peaks can be attributed to the Co−Co bond[51,55]. It can be obviously observed that the first characteristic peak of Cr_2-$MnCo_2O_4$ is significantly shifted to the right, indicating an increase in the Co−O distance. This shift tangibly confirms a change in the coordination environment at the Co active site.

By fitting the Tauc function to the K-M absorbance of the UV diffuse reflectance spectra shown in **Figure** 3g[56–58], the corresponding bandgap energies were first estimated to be 2.72, 2.66, and 2.62 eV for $MnCo_2O_4$, Cr_1-$MnCo_2O_4$, and Cr_2-$MnCo_2O_4$, respectively. Among them, Cr_2-$MnCo_2O_4$ has the smallest forbidden bandwidth, which indicates that the energy barrier to be overcome for internal electron transfer is smaller, which is consistent with theoretical calculations. Mott-Schottky measurements at a frequency of 2000 Hz were further used to characterize the semiconductor properties of the three samples. The Mott-Schottky plot provides access to the conduction band edge potential (CBM) through the flat band potential (E_{fb}) of the samples. It is noteworthy that the positive slope of the curves indicates that all three samples display n-type semiconductor properties, and the CBM of n-type semiconductors is often close to the value of E_{fb}. As shown in **Figure** 3h, $MnCo_2O_4$ has an E_{fb} of −1.58 V with respect to the Ag/AgCl electrode (−1.38 V with respect to the NHE, pH 7), whereas the E_{fb} of the n-type semiconductor is considered to be 0.1−0.2 V higher than the CBM, and

thus the CBM of $MnCo_2O_4$ with respect to the NHE is estimated to be −1.48 to −1.58 V. Considering the value of the bandgap, the calculated valence band edge potential (VBM) of $MnCo_2O_4$ with respect to NHE is +1.14 to +1.24 V. In the same way, the values of CBM relative to NHE are −1.32 to −1.42 V and VBM relative to NHE are +1.24 to +1.34 V for Cr_1-$MnCo_2O_4$ in **Figure** S12, and for Cr_2-$MnCo_2O_4$, the values of CBM relative to NHE are −1.38 to −1.48 V, and VBM relative to NHE are +1.14 to +1.24 V in **Figure** 3i. It can be seen that spinel electrocatalysts require lower excitation energies for the electrons to undergo the jump, which contributes to the transfer of electrons and accelerates the OER/ORR reaction kinetics.

During discharging and charging of LOBs, the electrochemical performance of three samples employed as cathode catalysts was investigated[1,59–61]. Firstly, the first complete discharge curve of Cr_2-$MnCo_2O_4$ at a current density of 100 mA g^{-1} shows a maximum discharge specific capacity of 16388.3 mAh g^{-1} (**Figure** 4a), which is superior to that of $MnCo_2O_4$ (9182.1 mAh g^{-1}) and Cr_1-$MnCo_2O_4$ (11827.5 mAh g^{-1}), revealing the optimum electrocatalytic activity. Furthermore, by comparing the three discharge/charge curves at a limiting capacity of 1000 mAh g^{-1} (**Figure** 4b), it is evident that the polarization voltage (0.77 V) of Cr_2-$MnCo_2O_4$ is significantly lower when compared to that of $MnCo_2O_4$ (1.06 V) and Cr_1-$MnCo_2O_4$ (0.87 V), suggesting that it possesses a superior Li_2O_2 decomposition kinetics. As depicted in **Figure** S13, it is worth noting that, in comparation of the cyclic voltammetry (CV) plots of the three samples, the total integrated area of Cr_2-$MnCo_2O_4$ is significantly larger than that of $MnCo_2O_4$ and Cr_1-$MnCo_2O_4$, suggesting that more discharge product is deposited and decomposed, which is highly consistent with the results of the first-charge discharge test. Also, the electrochemical impedance spectroscopy (EIS) was conducted on the three samples so as to further explore the reaction kinetics. In **Figure** 4c, a minimum value of charge transfer resistance (R_{ct}) was obtained for Cr_2-$MnCo_2O_4$ (79 Ω) compared to $MnCo_2O_4$ (136 Ω) and Cr_1-$MnCo_2O_4$ (93 Ω),

which indicates that Cr_2-$MnCo_2O_4$ promotes the charge transfer at the electrolyte/cathode interface, efficiently accelerating the OER/ORR reaction kinetics, in agreement with the experimental results of the narrowed the forbidden band width.

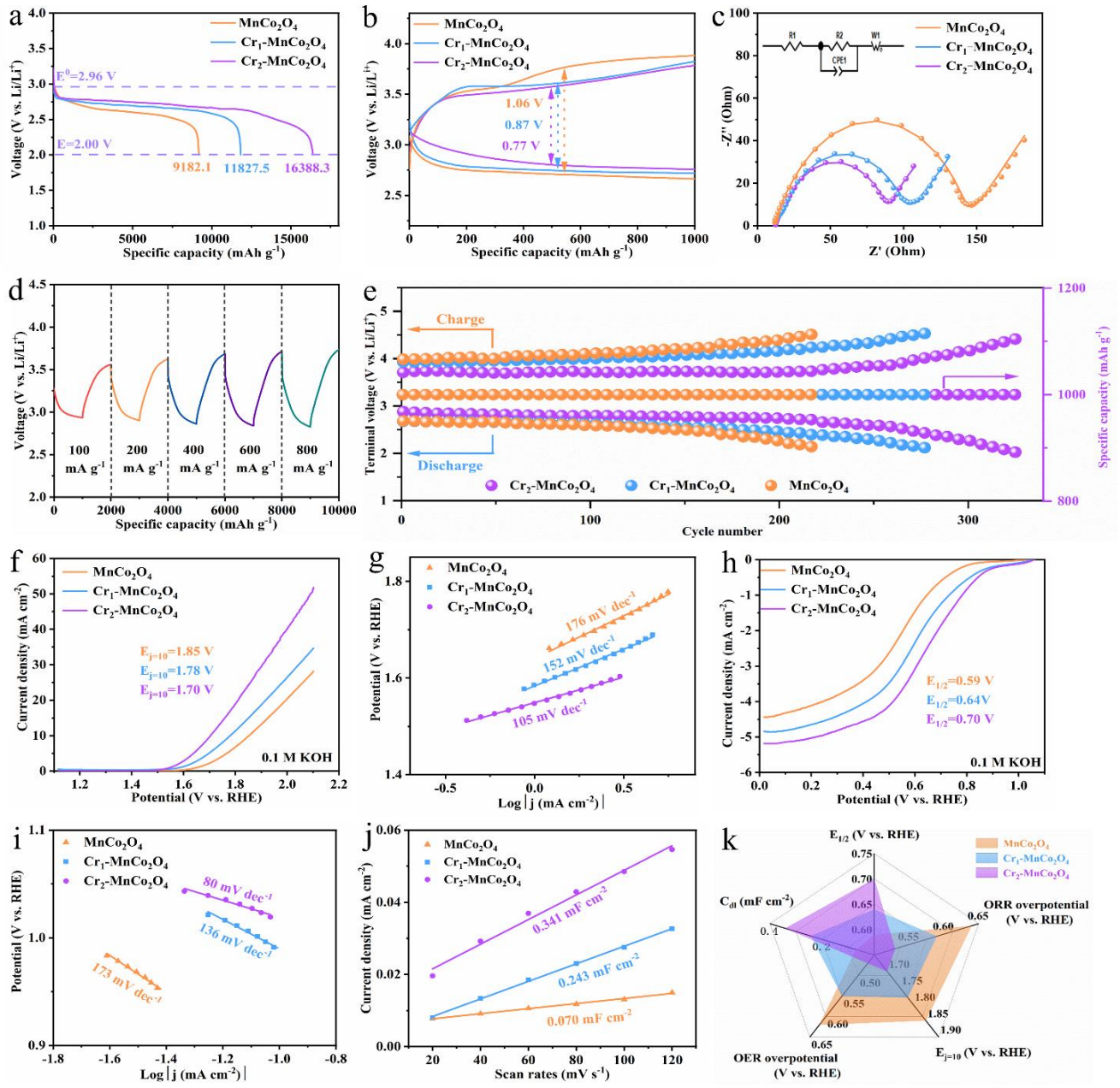

Figure 4. Electrochemical behaviors for $MnCo_2O_4$, Cr_1-$MnCo_2O_4$ and Cr_2-$MnCo_2O_4$. (a) Initial complete discharge curve. (b) Discharge/charge curve at a current density of 100 mA g^{-1} with a limiting capacity of 1000 mAh g^{-1}. (c) Nyquist plot. (d) Rate performance of Cr_2-$MnCo_2O_4$ with the limited capacity of 1000 mA h g^{-1} at different current densities from 100 mA g^{-1} to 800 mA g^{-1}. (e) Cyclic performance with a limited capacity of 1000 mAh g^{-1} at 200 mA g^{-1} (f) OER LSV polarization curves and the potential at 10 mA cm^{-2} ($E_{j=10}$). (g) Tafel slopes derived from OER curves. (h) ORR LSV polarization curves and half-wave potentials ($E_{1/2}$). (i) Tafel slopes derived from OER curves. (j) C_{dl} for $MnCo_2O_4$, Cr_1-$MnCo_2O_4$ and Cr_2-$MnCo_2O_4$. (k) The spider chart of catalysts performances in the aqueous solution system.

The rate performance of the three samples at different current densities as visualized in **Figure** 4d and **Figure** S14, depicts an increase in polarization of the corresponding LOBs with increasing current density. Notably, Cr_2-$MnCo_2O_4$ shows the slower rising overpotential and exhibits the lowest overpotential at all current densities, thus demonstrating promising electrocatalytic activity. The cycling performance of LOBs with the three samples as cathode catalysts was evaluated in **Figure** 4e. Cr_2-$MnCo_2O_4$ presents exceptional cycling stability, with the batteries lasting for 329 cycles. In contrast, until the voltage was increased to 4.5 V, $MnCo_2O_4$ and Cr_1-$MnCo_2O_4$ only lasted for 222 and 282 cycles, respectively. These results indicate that Cr_2-$MnCo_2O_4$ features favorable electrochemical reaction kinetics and excellent reversible properties for the formation and decomposition of discharge products.

The electrocatalytic performance of the three samples was evaluated in an aqueous system to verify the effectiveness and universality of spinel catalysts for electrocatalytic applications in various fields[62–64]. As shown in **Figure** 4f, the OER LSV curves for the three samples were clearly seen. One of them, Cr_2-$MnCo_2O_4$ has the smallest potential at 10 mA cm^{-2} ($E_{j=10}$=1.70 V), and the associated Tafel slope is likewise the smallest (**Figure** 4g), which suggests its higher OER activity. Similarly, in the ORR LSV curves (**Figure** 4h), it can be obtained that Cr_2-$MnCo_2O_4$ with the highest half-wave potential ($E_{1/2}$=0.70 V) and the lowest Tafel slope (**Figure** 4i) performs the optimal ORR activity. Notably, Cr_2-$MnCo_2O_4$ has the maximum double layer capacitance (C_{dl}) (0.341 mF cm^{-2}) in three samples (**Figure** 4j), indicating a larger active area, in agreement with the BET test results. These results demonstrate that the optimized Co-based spinel electrocatalysts exhibit favorable OER/ORR kinetics akin to the LOBs system, underscoring the exceptional electrocatalytic properties of spinel-type catalysts (**Figure** 4k).

To analyze the reversible deposition and decomposition kinetics of discharge products on the

cathode during the OER/ORR process in detail, the electrode surface morphology following discharge and charging was observed using SEM. As presented in **Figures** 5a-c, after discharge, embedded circular large nanosheet discharge products were generated on the $MnCo_2O_4$ electrode, and then a large number of small round sheet discharge products were stacked and grown on the Cr_1-$MnCo_2O_4$ electrode, and finally small particle discharge products were generated on the Cr_2-$MnCo_2O_4$ electrode. Each of the three samples had different discharge product morphologies, yet the variation trend was consistent with the predictions of theoretical calculations. The surface morphology of the electrodes after charging is exhibited in **Figures** 5d-f. There are round nanosheets on the $MnCo_2O_4$ electrode that have not been completely decomposed, and the discharge products accumulated on the Cr_1-$MnCo_2O_4$ electrode are similarly difficult to decompose completely. In contrast, the discharge products on the Cr_2-$MnCo_2O_4$ electrode are almost completely decomposed, showing excellent discharge product decomposition kinetics. The above results indicate that Cr_2-$MnCo_2O_4$ has excellent electrocatalytic properties and exhibits good deposition decomposition kinetics of discharge products, which is beneficial for prolonging the lifetime of LOBs.

To investigate the composition of the discharge products, XRD patterns of three samples were obtained at different stages in LOBs (**Figure** 5g)[65–67]. The XRD patterns of the three samples exhibit a characteristic peak at about 32.9°, corresponding to the (100) crystal plane of Li_2O_2 (JCPDS No. 09-0355), indicating that the discharge product is primarily Li_2O_2. Notably, the characteristic peak of Li_2O_2 on Cr_2-$MnCo_2O_4$ completely disappears after charging, confirming its high Li_2O_2 formation/decomposition reversibility. In comparison, the characteristic peak of Li_2O_2 is still present in the charged $MnCo_2O_4$, indicating incomplete decomposition of the discharge products, resulting in a poor reversibility of the electrochemical reaction. Moreover, it can be seen in **Figure** 5h, Fourier infrared spectroscopy (FT-IR) was applied to further examine the three electrodes. Compared with

$MnCo_2O_4$ and Cr_1-$MnCo_2O_4$, Cr_2-$MnCo_2O_4$ displays a series of characteristic absorption peaks after discharge, as follows, the peak at 860 cm^{-1} represents Li_2CO_3, while the peaks at 1190 and 1410 cm^{-1} signify the by-product CH_3COOLi, and the peaks at 1370 and 1630 cm^{-1} represent HCOOLi. Significantly, these characteristic peaks on Cr_2-$MnCo_2O_4$ largely disappear after charging, indicating excellent reversible properties that contribute to the enhanced electrochemical performance of LOBs.

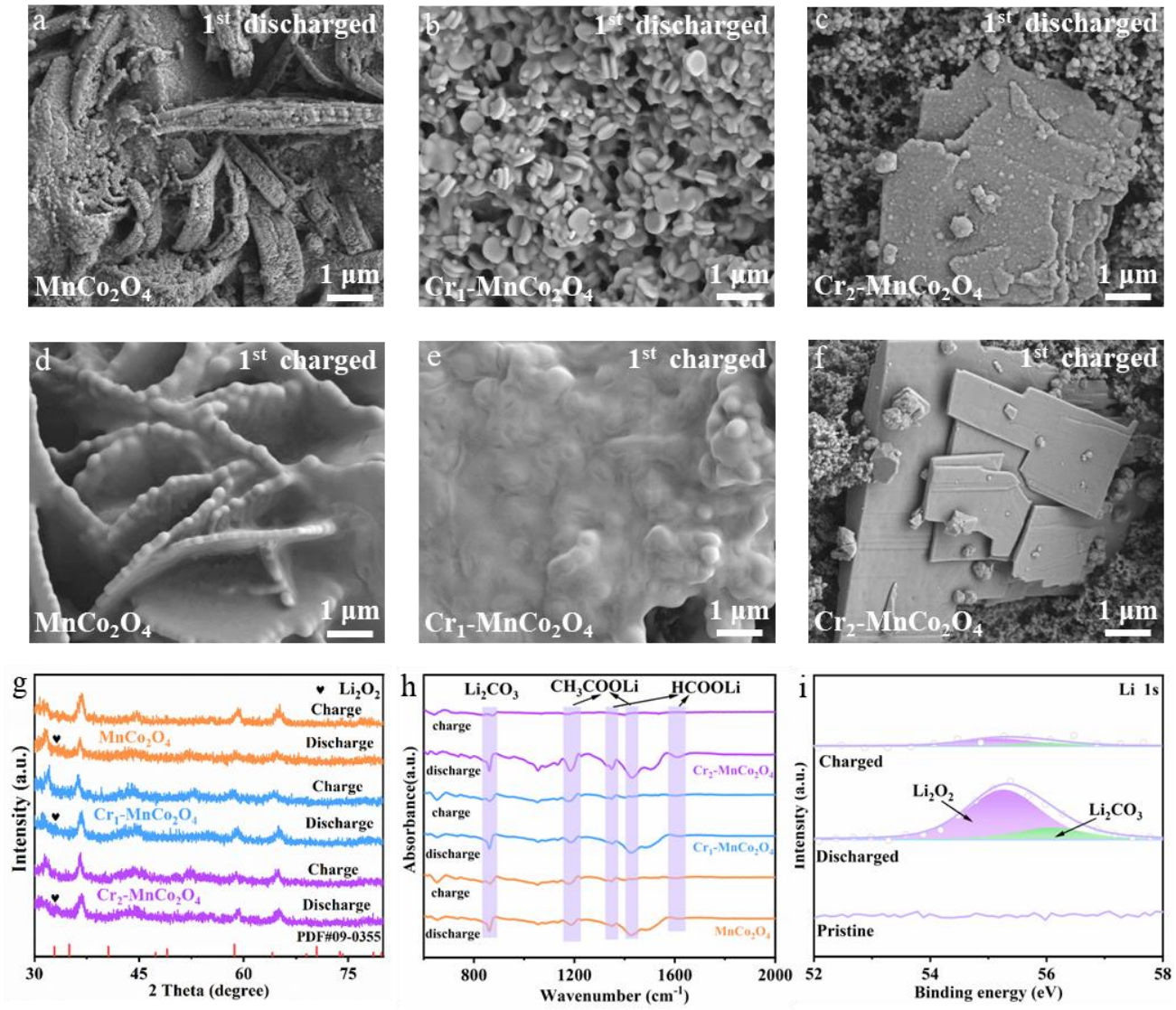

Figure 5. SEM images of $MnCo_2O_4$, Cr_1-$MnCo_2O_4$ and Cr_2-$MnCo_2O_4$ electrode (a-c) after discharged and (d-f) after charged. (g) XRD patterns of three electrodes at different stages. (h) FT-IR spectrum of three electrodes at different stages. (i) Li 1s XPS spectrum of Cr_2-$MnCo_2O_4$ at different stages.

XPS spectrum analyses were performed on three samples at different stages in LOBs to further explore the formation process and detailed composition of the discharge products[60,68,69]. The results,

as shown in **Figure** 5i and **Figure** S15, revealed distinctive peaks in the Li 1s XPS spectrum after discharge, corresponding to Li_2O_2 and Li_2CO_3. Upon charging, the peak areas of these characteristic peaks decreased, indicating the decomposition of the discharge products. However, a notable difference was observed between the Cr_2-$MnCo_2O_4$ electrode and the $MnCo_2O_4$ and Cr_1-$MnCo_2O_4$ electrodes, with the latter two exhibiting larger peak areas, suggesting incomplete discharge product decomposition and poorer electrochemical reversibility performance. Furthermore, the C 1s XPS spectrum comparison in **Figure** S16 facilitated the observation of discharge product formation and decomposition. Following discharge, a new peak corresponding to Li_2CO_3 formation emerged in the C 1s spectrum, likely due to an electrolyte-carbon cloth side reaction. Upon charging, the intensity of this peak decreased, indicating reversible discharge product decomposition. Notably, the Li_2CO_3 peak for Cr_2-$MnCo_2O_4$ decreased significantly upon charging, highlighting superior reversible performance. The EIS tests provided insight into the reversibility properties of the samples (**Figure** S17). Cr_2-$MnCo_2O_4$ exhibited a R_{ct} close to the initial stage after charging, suggesting highly reversible deposition and decomposition of discharge products, facilitating the OER/ORR reaction. Overall, the Cr_2-$MnCo_2O_4$ electrocatalyst demonstrates a crucial electrocatalytic role in LOBs, promoting Li_2O_2 deposition and decomposition kinetics, and showcasing exceptional reversibility and stability throughout the charge and discharge processes.

As displayed in **Figure** 6, the morphological changes occurred in the discharge products of the three samples during the charging and discharging process were clearly observed. Following the discharge process, embedded Li_2O_2 circular large nanosheets were present on the $MnCo_2O_4$ electrode surface, and a large number of Li_2O_2 circular small nanosheets were stacked and grown on the Cr_1-$MnCo_2O_4$ electrode, whereas small-size Li_2O_2 agglomerates were uniformly distributed on the Cr_2-$MnCo_2O_4$ electrode surface. It is well known that the morphology of the discharge products grown by

surface adsorption mechanism is normally in the form of thin films ($LiO_2^* + e^- + Li^+ \rightarrow Li_2O_2$), hence the discharge products were generated by solution-mediated mechanism on the three samples. Solution-mediated mechanism means that during the discharge process, the intermediate products generated by O_2 combined with Li^+ firstly dissolve and diffuse into the electrolyte ($LiO_{2(sol)}$). As the reaction proceeds, the $LiO_{2(sol)}$ aggregated in the electrolyte undergoes further disproportionation reactions, eventually forming Li_2O_2 agglomerates ($2LiO_{2(sol)} \rightarrow Li_2O_2 + O_2$), in line with the above morphological results[8,59,70].

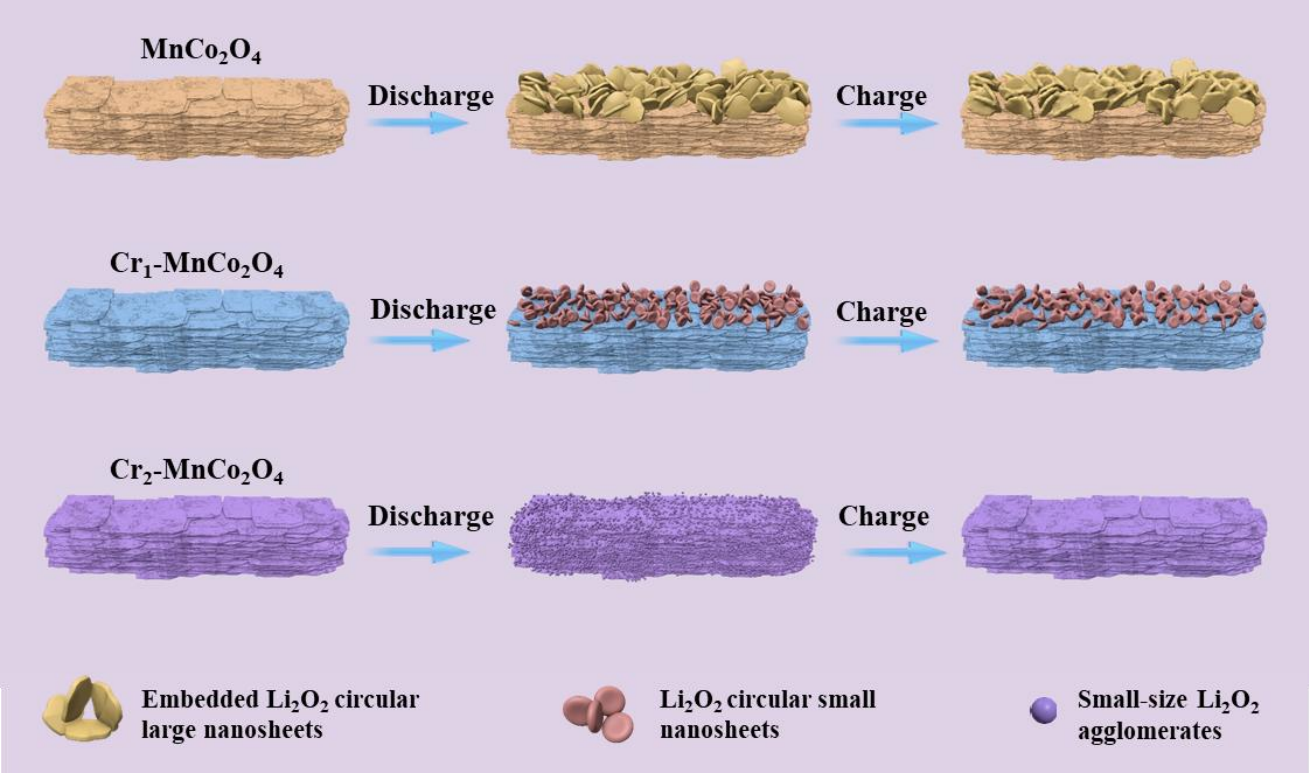

Figure 6. Schematic illustrations of the ORR (discharge) and OER (charge) process for three samples.

In determining the particular surface morphology of three samples, the adsorption behavior of the Co active sites on the oxygen-containing intermediates emerges as the fundamental factor, despite the consistent growth mechanisms of Li_2O_2. The higher adsorption capacity of Cr_2-$MnCo_2O_4$ leads to an increased number of Li_2O_2 nucleation sites on the cathode surface, expanding the range of disproportionation reactions for $LiO_{2(sol)}$ concentrated around these sites. Consequently, this facilitates the homogeneous growth of small-sized Li_2O_2 agglomerates. The large contact area between these

uniformly grown agglomerates and the cathode surface enhances charge transfer, boosting the electrocatalytic effect of the Co active sites and thereby significantly aiding the reversible Li_2O_2 deposition and decomposition kinetics. Conversely, when the adsorption capacity is lower, there are fewer Li_2O_2 nucleation sites on the cathode surface, leading $LiO_{2(sol)}$ to undergo disproportionation reactions in a limited nucleation region. This results in the formation of larger-size Li_2O_2 agglomerates, such as embedded Li_2O_2 circular large nanosheets on $MnCo_2O_4$ and Li_2O_2 circular small nanosheets on Cr_1-$MnCo_2O_4$. These larger agglomerates are challenging to completely decompose, resulting in higher charging voltages. Additionally, their narrower contact area with the cathode surface hinders charge transfer, unfavorably impacting the OER/ORR reaction kinetics. In summary, the excellent electrochemical performance of the LOBs is closely tied to the Li_2O_2 morphology on the Cr_2-$MnCo_2O_4$ electrode. Specifically, the optimization of the Co−O covalency of the Cr_2-$MnCo_2O_4$ electrocatalyst enhances the catalytic activity of the Co active site in regulating the OER/ORR reactions. This optimization effectively promotes the reversible formation and decomposition of Li_2O_2/LiO_2, thereby significantly enhancing the electrochemical performance of LOBs.

CONCLUSIONS

In summary, a highly efficient Cr_2-$MnCo_2O_4$ electrocatalyst was successfully prepared by incorporating an appropriate amount of Cr^{3+}, which effectively enhances the electrocatalytic performance of the Co active site, thereby leading to an improvement in the LOBs electrochemical performance. DFT calculations reveal that the introduction of Cr^{3+} results in a decrease in the charge transfer energy between the Co 3d and O 2p orbitals, along with an enhancement in Co−O covalency within the Cr_2-$MnCo_2O_4$ spinel structure. These structural modifications not only strengthen electronic interactions and promote electron transfer, but also enhance the electrocatalytic activity of the active

site and optimize the adsorption towards oxygen-containing intermediates. Consequently, the surface of Cr_2-$MnCo_2O_4$ promotes the uniform growth of small Li_2O_2 agglomerates, leading to remarkable deposition and decomposition kinetics of Li_2O_2/LiO_2 and a significant enhancement in the electrochemical performance of LOBs. As a result, Cr_2-$MnCo_2O_4$-based LOBs demonstrate an exceptional specific discharge capacity of 16388.3 mAh g^{-1} and superior cycling stability over 329 cycles. This study holds great importance in guiding the development of advanced high-efficiency spinel electrocatalysts and the future realization of high-performance LOBs for practical applications.

METHODS AND EXPERIMENTAL SECTION

Materials synthesis. $Mn(NO_3)_2{\cdot}4H_2O$ (AR, 99%), $Co(NO_3)_2{\cdot}6H_2O$ (AR, 99%), $Cr(NO_3)_3{\cdot}9H_2O$ (AR, 99%) and $CO(NH_2)_2$ (AR, 99%) were purchased from Chron Chemicals (Chengdu, China).

$MnCo_2O_4$ synthesis: Typically, 1 mmol $Mn(NO_3)_2{\cdot}4H_2O$ and 2 mmol $Co(NO_3)_2{\cdot}6H_2O$ and 12 mmol $CO(NH_2)_2$ were dissolved in deionized water (60 ml) and agitated to a well-dispersed solution. Then the homogeneous solution was transferred to a 100 ml Teflon lined autoclave and heat-treated at 180 °C for 12 h. After that, the resulting precursor was scrubbed repeatedly with deionized water and ethanol and dried at 70 °C overnight. Eventually, $MnCo_2O_4$ was obtained after calcination at 400°C for 3 h.

Cr-$MnCo_2O_4$ synthesis: 1 mmol $Mn(NO_3)_2{\cdot}4H_2O$ and 0.3 (0.5) mmol $Cr(NO_3)_2{\cdot}9H_2O$, 1.7 (1.5) mmol $Co(NO_3)_2{\cdot}6H_2O$ and 12 mmol $CO(NH_2)_2$ were dissolved in deionized water (60 ml) and agitated to a well-dispersed solution. Then the homogeneous solution was transferred to a 100 ml Teflon lined autoclave and heat-treated at 180 °C for 12 h. After that, the resulting precursor was scrubbed repeatedly with deionized water and ethanol and dried at 70 °C overnight. Eventually, Cr_1-$MnCo_2O_4$ ($MnCr_{0.3}Co_{1.7}O_4$) and Cr_2-$MnCo_2O_4$ ($MnCr_{0.5}Co_{1.5}O_4$) was obtained after calcination at 400°C for 3 h.

Materials characterization. SEM (ZEISS Gemini SEM 300) and EDS (Smartedx) were used for surface morphology and elemental composition characterization. TEM (FEI Tecnai G2 F20) was utilized to observe the microstructure. XRD (D/MAX-IIIC) was applied to measure the crystal structure. ICP-OES (Agilent 5110) was used to check the specific elemental content. XPS (Thermo

Scientific K-Alpha) was adopted to feature the surface chemical state and composition. The Micromeritics ASAP 2460 was applied to evaluate the nitrogen adsorption-desorption isotherm. Raman spectra (Thermo Scientific DXR) were obtained with an excitation wavelength at 532 nm. FT-IR (Nicolet iS50) was conducted to examine the specific composition of the discharge products. X-ray absorption fine structure spectroscopy was carried out using the Rapid XAFS 2M (Anhui Absorption Spectroscopy Analysis Instrument Co., Ltd.) by transmission (or fluorescence) mode at 20 kV and 20 mA, and the Si (533) spherically bent crystal analyzer with a radius of curvature of 500 mm was used for Co.

Electrochemical measurements. A slurry of as-prepared samples, Super P carbon and polyvinylidene fluoride in N-Methyl pyrrolidone mixed in a weight ratio of 8:1:1, was coated on carbon cloth of 16 mm diameter and dried to prepare an oxygen cathode of 1 mg cm^{-2}. Next, in a glove box filled with Ar, LOB containing an oxygen electrode, glass fiber separator (GF/D), a Li anode and electrolyte (1 M LiTFSI in TEGDME (100 Vol %)) was assembled. All assembled 2032 type coin cells were measured with the LAND CT 2001A battery tester with voltage limits of 2.0 to 4.5 V. On Bio-Logic SP-150 electrochemical workstation, the cyclic voltammetry (CV) measurement, a scan rate of 1 mV s^{-1} at voltages ranging from 2.0 to 4.5 V was performed and electrochemical impedance spectroscopy (EIS) was evaluated over a frequency range of 100 kHz to 0.01 Hz at 5 mV voltage amplitude.

The ORR/OER property variation trend among as-prepared samples was predicted using a

rotating disk electrode experiment in a standard three-electrode system consisting of a platinum (Pt) wire counter electrode, a Hg/HgO reference electrode, a 5 mm diameter glassy carbon (GC) working electrode and the electrolyte (0.1 M KOH). The desired slurry was prepared by homogeneously dispersing the sample (4 mg) and Super P (1 mg) in 60 μl Nafion (5 wt%), 470 μl deionized water and 470 μl ethanol. Then, 10μl slurry was applied to the GC electrode and dried spontaneously to initiate the electrochemical performance measurement. Linear scanning voltammetry (LSV) curves of the ORR in O_2-saturated electrolyte with a scan rate of 5 mV s^{-1} and a rotational speed of 1600 rpm were tested from 0.25 ~ −0.85 V (vs. Hg/HgO). LSV curves of the OER in N_2-saturated electrolyte with a scan rate of 5 mV s^{-1} and a rotational speed of 1600 rpm were tested from 0.25 to 1.25 V (vs. Hg/HgO). In addition, all electrocatalysts were activated for 20 times via cyclic voltammetry prior to testing, at a rotation speed of 1600 rpm and a scan rate of 100 mV s^{-1}.

All potentials were converted to reversible hydrogen electrode (RHE) scales after IR correction according to the following equation

$$E_{RHE} = E_{Hg/HgO} + 0.0591 \times PH + E^0_{Hg/HgO} + IR$$

In which $E_{Hg/HgO}$ is defined as the measured potential, $E^0_{Hg/HgO} = 0.098$ V, R denotes the solution resistance.

The electrochemically active surface area (ECSA) size was indirectly expressed by the double layer capacitance (C_{dl}). A serious of CV measurements in the non-Faradaic region (−0.05-0.05 V (*vs.* Hg/HgO)) at scan rates of 20, 40, 60, 80, 100 and 120 mV s^{-1} were performed, and then obtained C_{dl} via calculating the slope of the fitted straight line $\Delta J=(J_a-J_c)/2$ with respect to the scan rate (J_a/J_c equals the anodic/cathodic current at 0 V (*vs.* Hg/HgO)).

Theoretical calculation. The detailed description can be found in the Supporting Information.

SUPPORTING INFORMATION

Corresponding theoretical section. **Figure** S1-S6. DFT calculation; **Figure** S7. XRD analysis; **Figure** S8-S9. SEM images; **Figure** S10. N_2 adsorption/ desorption isotherm curves and pore size distribution; **Figure** S11. High-resolution XPS spectra of Mn 2p, O 1s; **Figure** S12. Mott-Schottky plots; **Figure** S13. Cyclic voltammetry curve; **Figure** S14. Rate performance; **Figure** S15-S16. High-resolution XPS spectra of Li 1s, C 1s at different stages; **Figure** S17. Nyquist plots; **Table** S1. ICOHP values; **Table** S2. ICP-OES analysis; **Table** S3. Specific surface area analysis.

AUTHOR CONTRIBUTIONS

Yu Pan: Visualization, Conceptualization, Methodology, Writing–original draft. **Anjun Hu:** Investigation, Validation, Formal analysis. **Ruizhe Xu:** Investigation. **Kun Li:** Investigation. **Ting Li:** Investigation. **Jingze Chen:** Investigation. **Borui Yang:** Investigation. **Yuanjian Li:** Formal analysis. **Zhi Wei Seh:** Investigation, Validation, Formal analysis. **Jianping Long:** Writing – review & editing, Funding acquisition, Project administration, Supervision.

NOTES

The authors declare no competing financial interest.

ACKNOWLEDGMENTS

The authors acknowledge the National Natural Science Foundation of China (21805018; 52002039), the Natural Science Foundation of Sichuan Province (24NSFSC1365), and Scientific Research Startup Foundation of Chengdu University of Technology (10912-KYQD2023-10240), the Agency for Science, Technology and Research (MTC Programmatic Fund M23L9b0052), and the Singapore National Research Foundation (NRF Investigatorship NRF-NRFI09-0002). We also acknowledge the Anhui Absorption Spectroscopy Analysis Instrument Co, Ltd. for XAFS measurements and analysis.

REFERENCES

(1) Ahn, S.; Zor, C.; Yang, S.; Lagnoni, M.; Dewar, D.; Nimmo, T.; Chau, C.; Jenkins, M.; Kibler, A. J.; Pateman, A.; Rees, G. J.; Gao, X.; Adamson, P.; Grobert, N.; Bertei, A.; Johnson, L. R.; Bruce, P. G. Why Charging Li–Air Batteries with Current Low-Voltage Mediators Is Slow and Singlet Oxygen Does Not Explain Degradation. *Nat. Chem.* **2023**. *15*, 1022–1029. https://doi.org/10.1038/s41557-023-01203-3.
(2) Liu, T.; Vivek, J. P.; Zhao, E. W.; Lei, J.; Garcia-Araez, N.; Grey, C. P. Current Challenges and Routes Forward for Nonaqueous Lithium–Air Batteries. *Chem. Rev.* **2020**, *120* (14), 6558–6625. https://doi.org/10.1021/acs.chemrev.9b00545.
(3) Zhao, Z.-J.; Liu, S.; Zha, S.; Cheng, D.; Studt, F.; Henkelman, G.; Gong, J. Theory-Guided Design of Catalytic Materials Using Scaling Relationships and Reactivity Descriptors. *Nat. Rev. Mater.* **2019**, *4* (12), 792–804. https://doi.org/10.1038/s41578-019-0152-x.
(4) Du, Y.; Li, B.; Xu, G.; Wang, L. Recent Advances in Interface Engineering Strategy for Highly-efficient Electrocatalytic Water Splitting. *InfoMat.* **2023**, *5* (1), e12377. https://doi.org/10.1002/inf2.12377.
(5) Shu, C.; Wang, J.; Long, J.; Liu, H.; Dou, S. Understanding the Reaction Chemistry during Charging in Aprotic Lithium–Oxygen Batteries: Existing Problems and Solutions. *Adv. Mater.* **2019**, *31* (15), 1804587. https://doi.org/10.1002/adma.201804587.
(6) Xu, C.; Ge, A.; Kannari, K.; Peng, B.; Xue, M.; Ding, B.; Inoue, K.; Zhang, X.; Ye, S. The Decisive Role of Li_2O_2 Desorption for Oxygen Reduction Reaction in Li–O_2 Batteries. *ACS Energy Lett.* **2023**, 8, 1289–1299. https://doi.org/10.1021/acsenergylett.2c02714.
(7) Chen, D.; Yu, R.; Lu, R.; Pu, Z.; Wang, P.; Zhu, J.; Ji, P.; Wu, D.; Wu, J.; Zhao, Y.; Kou, Z.; Yu, J.; Mu, S. Tunable RU-RU_2P Heterostructures with Charge Redistribution for Efficient PH-UNIVERSAL Hydrogen Evolution. *InfoMat* **2022**, *4* (5), e12287. https://doi.org/10.1002/inf2.12287.
(8) Liu, L.; Liu, Y.; Wang, C.; Peng, X.; Fang, W.; Hou, Y.; Wang, J.; Ye, J.; Wu, Y. Li_2O_2 Formation Electrochemistry and Its Influence on Oxygen Reduction/Evolution Reaction Kinetics in Aprotic Li–O_2 Batteries. *Small Methods* **2022**, *6* (1), 2101280. https://doi.org/10.1002/smtd.202101280.
(9) Song, L.-N.; Zhang, W.; Wang, Y.; Ge, X.; Zou, L.-C.; Wang, H.-F.; Wang, X.-X.; Liu, Q.-C.; Li, F.; Xu, J.-J. Tuning Lithium-Peroxide Formation and Decomposition Routes with Single-Atom Catalysts for Lithium–Oxygen Batteries. *Nat. Commun.* **2020**, *11* (1), 2191. https://doi.org/10.1038/s41467-020-15712-z.
(10) Wang, P.; Zhao, D.; Hui, X.; Qian, Z.; Zhang, P.; Ren, Y.; Lin, Y.; Zhang, Z.; Yin, L. Bifunctional Catalytic Activity Guided by Rich Crystal Defects in Ti_3C_2 MXene Quantum Dot Clusters for Li–O_2 Batteries. *Adv. Energy Mater.* **2021**, *11* (32), 2003069. https://doi.org/10.1002/aenm.202003069.
(11) Zhou, Y.; Sun, S.; Wei, C.; Sun, Y.; Xi, P.; Feng, Z.; Xu, Z. J. Significance of Engineering the Octahedral Units to Promote the Oxygen Evolution Reaction of Spinel Oxides. *Adv. Mater.* **2019**, *31* (41), 1902509. https://doi.org/10.1002/adma.201902509.
(12) Wei, C.; Feng, Z.; Scherer, G. G.; Barber, J.; Shao-Horn, Y.; Xu, Z. J. Cations in Octahedral Sites: A Descriptor for Oxygen Electrocatalysis on Transition-Metal Spinels. *Adv. Mater.* **2017**, *29* (23), 1606800. https://doi.org/10.1002/adma.201606800.
(13) Wang, X.; Luo, J.; Tuo, Y.; Gu, Y.; Liu, W.; Wang, S.; Zhou, Y.; Zhang, J. Hierarchical Heterostructure of NiFe2O4 Nanoflakes Grown on the Tip of $NiCo_2O_4$ Nanoneedles with Enhanced Interfacial Polarization Effect to Achieve Highly Efficient Electrocatalytic Oxygen Evolution. *Chem. Eng. J.* **2023**, *457*, 141169. https://doi.org/10.1016/j.cej.2022.141169.
(14) Wang, Z.; Huang, J.; Wang, L.; Liu, Y.; Liu, W.; Zhao, S.; Liu, Z. Cation-Tuning Induced d-Band

Center Modulation on Co-Based Spinel Oxide for Oxygen Reduction/Evolution Reaction. *Angew. Chem. Int. Ed.* **2022**, *61* (16), e202114696. https://doi.org/10.1002/anie.202114696.
(15) Moon, J.; Beker, W.; Siek, M.; Kim, J.; Lee, H. S.; Hyeon, T.; Grzybowski, B. A. Active Learning Guides Discovery of a Champion Four-Metal Perovskite Oxide for Oxygen Evolution Electrocatalysis. *Nat. Mater.* **2023,** 23,108–115. https://doi.org/10.1038/s41563-023-01707-w.
(16) Sun, Y.; Liao, H.; Wang, J.; Chen, B.; Sun, S.; Ong, S. J. H.; Xi, S.; Diao, C.; Du, Y.; Wang, J.-O.; Breese, M. B. H.; Li, S.; Zhang, H.; Xu, Z. J. Covalency Competition Dominates the Water Oxidation Structure–Activity Relationship on Spinel Oxides. *Nat. Catal.* **2020**, *3* (7), 554–563. https://doi.org/10.1038/s41929-020-0465-6.
(17) Liang, Y.; Wang, H.; Zhou, J.; Li, Y.; Wang, J.; Regier, T.; Dai, H. Covalent Hybrid of Spinel Manganese−Cobalt Oxide and Graphene as Advanced Oxygen Reduction Electrocatalysts. *J. Am. Chem. Soc.* **2012**. 134, 3517−3523. https://doi.org/10.1021/ja210924t.
(18) Wang, J.; Zhang, J.; Zhang, L.; Chen, L.; He, G.; Jiang, H. Modulating Metal-Oxygen Interactions of High-Entropy Oxide Electrocatalysts Enables Highly-Active and Ultra-Stable Water Oxidation. *Appl. Catal. B Environ.* **2024**, *342*, 123382. https://doi.org/10.1016/j.apcatb.2023.123382.
(19) Wang, X.; Raghupathy, R. K. M.; Querebillo, C. J.; Liao, Z.; Li, D.; Lin, K.; Hantusch, M.; Sofer, Z.; Li, B.; Zschech, E.; Weidinger, I. M.; Kühne, T. D.; Mirhosseini, H.; Yu, M.; Feng, X. Interfacial Covalent Bonds Regulated Electron-Deficient 2D Black Phosphorus for Electrocatalytic Oxygen Reactions. *Adv. Mater.* **2021**, *33* (20), 2008752. https://doi.org/10.1002/adma.202008752.
(20) Lv, Q.; Zhu, Z.; Ni, Y.; Geng, J.; Li, F. Spin-State Manipulation of Two-Dimensional Metal–Organic Framework with Enhanced Metal–Oxygen Covalency for Lithium-Oxygen Batteries. *Angew. Chem. Int. Ed.* **2022**, *61* (8), e202114293. https://doi.org/10.1002/anie.202114293.
(21) Gao, X.; Liu, J.; Sun, Y.; Wang, X.; Geng, Z.; Shi, F.; Wang, X.; Zhang, W.; Feng, S.; Wang, Y.; Huang, K. Optimized $Co^{2+}_{(Td)}$–O–$Fe^{3+}_{(Oh)}$ Electronic States in a Spinel Electrocatalyst for Highly Efficient Oxygen Evolution Reaction Performance. *Inorg. Chem. Front.* **2019**, *6* (11), 3295–3301. https://doi.org/10.1039/C9QI00852G.
(22) Zhao, X.; Li, X.; An, L.; Zheng, L.; Yang, J.; Wang, D. Controlling the Valence-Electron Arrangement of Nickel Active Centers for Efficient Hydrogen Oxidation Electrocatalysis. *Angew. Chem. Int. Ed.* **2022**. e202206588. https://doi.org/10.1002/anie.202206588.
(23) Wang, X.; Du, D.; Xu, H.; Yan, Y.; Wen, X.; Ren, L.; Shu, C. NiMn-Based Metal-Organic Framework with Optimized Eg Orbital Occupancy as Efficient Bifunctional Electrocatalyst for Lithium-Oxygen Batteries. *Chem. Eng. J.* **2023**, *452*, 139524. https://doi.org/10.1016/j.cej.2022.139524.
(24) Wu, Y.; Ding, H.; Yang, T.; Xia, Y.; Zheng, H.; Wei, Q.; Han, J.; Peng, D.; Yue, G. Composite $NiCo_2O_4$@CeO_2 Microsphere as Cathode Catalyst for High-Performance Lithium–Oxygen Battery. *Adv. Sci.* **2022**, *9* (17), 2200523. https://doi.org/10.1002/advs.202200523.
(25) Li, D.; Zhao, L.; Wang, J.; Yang, C. Tailoring the d-Band Center over Isomorphism Pyrite Catalyst for Optimized Intrinsic Affinity to Intermediates in Lithium–Oxygen Batteries. *Adv. Energy Mater.***2023**, 2204057. https://doi.org/10.1002/aenm.202204057.
(26) Hwang, J.; Rao, R. R.; Giordano, L.; Katayama, Y.; Yu, Y.; Shao-Horn, Y. Perovskites in Catalysis and Electrocatalysis. *Science* **2017**, *358* (6364), 751–756. https://doi.org/10.1126/science.aam7092.
(27) Suntivich, J.; Gasteiger, H. A.; Yabuuchi, N.; Nakanishi, H.; Goodenough, J. B.; Shao-Horn, Y. Design Principles for Oxygen-Reduction Activity on Perovskite Oxide Catalysts for Fuel Cells and Metal–Air Batteries. *Nat. Chem.* **2011**, *3* (7), 546–550. https://doi.org/10.1038/nchem.1069.
(28) Xiao, M.; Zhu, J.; Li, S.; Li, G.; Liu, W.; Deng, Y.-P.; Bai, Z.; Ma, L.; Feng, M.; Wu, T.; Su, D.;

Lu, J.; Yu, A.; Chen, Z. 3d-Orbital Occupancy Regulated Ir-Co Atomic Pair Toward Superior Bifunctional Oxygen Electrocatalysis. *ACS Catal.* **2021**, *11* (14), 8837–8846. https://doi.org/10.1021/acscatal.1c02165.
(29) Shen, Z.; Cao, M.; Wen, Y.; Li, J.; Zhang, X.; Hui, J.; Zhu, Q.; Zhang, H. Tuning the Local Coordination of $CoP_{1-x}S_x$ between NiAs- and MnP-Type Structures to Catalyze Lithium–Sulfur Batteries. *ACS Nano* **2023**, 17(3), 3143–3152. https://doi.org/10.1021/acsnano.2c12436.
(30) Pan, Y.; Li, K.; Hu, A.; Zhao, C.; Zhang, Y.; Jiang, X.; Li, B.; Wang, J.; Long, J. Manipulating Li_2O_2 Deposition Morphology by Surface Spin Modulation of Cobalt-Based Spinel Oxide Catalysts in Lithium−oxygen Batteries. *Chem. Eng. J.* **2023**, *477*, 147209. https://doi.org/10.1016/j.cej.2023.147209.
(31) Zhao, C.; Yan, Z.; Zhou, B.; Pan, Y.; Hu, A.; He, M.; Liu, J.; Long, J. Identifying the Role of Lewis-base Sites for the Chemistry in Lithium-Oxygen Batteries. *Angew. Chem. Int. Ed.* **2023**, *62* (32), e202302746. https://doi.org/10.1002/anie.202302746.
(32) Zheng, R.; Shu, C.; Chen, X.; Yan, Y.; He, M.; Du, D.; Ren, L.; Hu, A.; Long, J. Unique Intermediate Adsorption Enabled by Anion Vacancies in Metal Sulfide Embedded MXene Nanosheets Overcoming Kinetic Barriers of Oxygen Electrode Reactions in Lithium-Oxygen Batteries. *Energy Storage Mater.* **2021**, *40*, 41–50. https://doi.org/10.1016/j.ensm.2021.04.041.
(33) Wu, D.; Wu, S.; Zhang, G.; Hui, C.; Cao, D.; Guo, S.; Feng, H.; Wang, Q.; Cheng, S.; Cui, P.; Yang, Z. Boosting Li–O_2 Battery Performance via Coupling of P–N Site-Rich N, P Co-Doped Graphene-Like Carbon Nanosheets with Nano-$CePO_4$. *Small* **2023**, *19* (19), 2206455. https://doi.org/10.1002/smll.202206455.
(34) Zhang, G.; Liu, C.; Guo, L.; Liu, R.; Miao, L.; Dang, F. Electronic “Bridge” Construction via Ag Intercalation to Diminish Catalytic Anisotropy for 2D Tin Diselenide Cathode Catalyst in Lithium–Oxygen Batteries. *Adv. Energy Mater.* **2022**, *12* (27), 2200791. https://doi.org/10.1002/aenm.202200791.
(35) Huang, H.; Cheng, C.; Zhang, G.; Guo, L.; Li, G.; Pan, M.; Dang, F.; Mai, X. Surface Phosphatization for a Sawdust-Derived Carbon Catalyst as Kinetics Promoter and Corrosion Preventer in Lithium–Oxygen Batteries. *Adv. Funct. Mater.* **2022**, 2111546. https://doi.org/10/gpjcpj.
(36) Khan, M. U.; Wang, L.; Liu, Z.; Gao, Z.; Wang, S.; Li, H.; Zhang, W.; Wang, M.; Wang, Z.; Ma, C.; Zeng, J. Pt_3Co Octapods as Superior Catalysts of CO_2 Hydrogenation. *Angew. Chem. Int. Ed.* **2016**, *55* (33), 9548–9552. https://doi.org/10.1002/anie.201602512.
(37) Xia, Q.; Zhao, L.; Zhang, Z.; Wang, J.; Li, D.; Han, X.; Zhou, Z.; Long, Y.; Dang, F.; Zhang, Y.; Chou, S. $MnCo_2S_4$-$CoS_{1.097}$ Heterostructure Nanotubes as High Efficiency Cathode Catalysts for Stable and Long-Life Lithium-Oxygen Batteries Under High Current Conditions. *Adv. Sci.* **2021**, *8* (22), 2103302. https://doi.org/10.1002/advs.202103302.
(38) Zhang, Y.; Li, G.; Zhao, Z.; Han, L.; Feng, Y.; Liu, S.; Xu, B.; Liao, H.; Lu, G.; Xin, H. L.; Huang, X. Atomically Isolated Rh Sites within Highly Branched Rh_2Sb Nanostructures Enhance Bifunctional Hydrogen Electrocatalysis. *Adv. Mater.* **2021**, *33* (43), 2105049. https://doi.org/10.1002/adma.202105049.
(39) Yuan, H.; Ma, X.; Xu, Z. Pore Structure Analysis of PFSA/SiO_2 Composite Catalysts from Nitrogen Adsorption Isotherms. *Sci. China Chem.* **2011**, *54* (1), 257–262. https://doi.org/10.1007/s11426-010-4185-7.
(40) Baldovino-Medrano, V. G.; Niño-Celis, V.; Isaacs Giraldo, R. Systematic Analysis of the Nitrogen Adsorption–Desorption Isotherms Recorded for a Series of Materials Based on Microporous–Mesoporous Amorphous Aluminosilicates Using Classical Methods. *J. Chem. Eng. Data* **2023**, *68* (9), 2512–2528. https://doi.org/10.1021/acs.jced.3c00257.

(41) Qi, Y.; Xiao, X.; Mei, Y.; Xiong, L.; Chen, L.; Lin, X.; Lin, Z.; Sun, S.; Han, B.; Yang, D.; Qin, Y.; Qiu, X. Modulation of Brønsted and Lewis Acid Centers for $Ni_xCo_{3-x}O_4$ Spinel Catalysts: Towards Efficient Catalytic Conversion of Lignin. *Adv. Funct. Mater.* **2022**, *32* (15), 2111615. https://doi.org/10.1002/adfm.202111615.
(42) Liu, S.; Zhang, B.; Cao, Y.; Wang, H.; Zhang, Y.; Zhang, S.; Li, Y.; Gong, H.; Liu, S.; Yang, Z.; Sun, J. Understanding the Effect of Nickel Doping in Cobalt Spinel Oxides on Regulating Spin State to Promote the Performance of the Oxygen Reduction Reaction and Zinc–Air Batteries. *ACS Energy Lett.* **2023**, *8* (1), 159–168. https://doi.org/10.1021/acsenergylett.2c02457.
(43) Yadav, N.; Khamsanga, S.; Kheawhom, S.; Qin, J.; Pattananuwat, P. $MnCo_2O_4$ Spinel Microsphere Assembled with Flake Structure as a Cathode for High-Performance Zinc Ion Battery. *J. Energy Storage* **2023**, *64*, 107148. https://doi.org/10.1016/j.est.2023.107148.
(44) Li, Y.; Qin, J.; Ding, Y.; Ma, J.; Das, P.; Liu, H.; Wu, Z.-S.; Bao, X. Two-Dimensional Mn_3O_4 Nanosheets with Dominant (101) Crystal Planes on Graphene as Efficient Oxygen Catalysts for Ultrahigh Capacity and Long-Life Li–O_2 Batteries. *ACS Catal.* **2022**, *12* (20), 12765–12773. https://doi.org/10.1021/acscatal.2c02544.
(45) Shi, Q.; Shen, B.; Zhang, X.; Lyu, H.; Wang, J.; Li, S.; Kang, D. Insights into Synergistic Oxidation Mechanism of Hg0 and Chlorobenzene over $MnCo_2O_4$ Microsphere with Oxygen Vacancy and Acidic Site. *Journal of Hazardous Materials* **2023**, *443*, 130179. https://doi.org/10.1016/j.jhazmat.2022.130179.
(46) Fan, Y.; Li, R.; Zhao, C.; Hu, A.; Zhou, B.; Pan, Y.; Chen, J.; Yan, Z.; Liu, M.; He, M.; Liu, J.; Chen, N.; Long, J. Chromium-Doped Inverse Spinel Electrocatalysts with Optimal Orbital Occupancy for Facilitating Reaction Kinetics of Lithium-Oxygen Batteries. *J. Colloid Interface Sci.* **2023**, *645*, 439–447. https://doi.org/10.1016/j.jcis.2023.04.128.
(47) Feng, C.; Chen, C.; Xiong, G.; Yang, D.; Wang, Z.; Pan, Y.; Fei, Z.; Lu, Y.; Liu, Y.; Zhang, R.; Li, X. Cr-Doping Regulates Mn3O4 Spinel Structure for Efficient Total Oxidation of Propane: Structural Effects and Reaction Mechanism Determination. *Appl. Catal. B Environ.* **2023**, *328*, 122528. https://doi.org/10.1016/j.apcatb.2023.122528.
(48) Jiang, Z.; Wen, K.; Song, C.; Liu, T.; Dong, Y.; Liu, M.; Deng, C.; Deng, C.; Yang, C. Highly Conductive Mn-Co Spinel Powder Prepared by Cu-Doping Used for Interconnect Protection of SOFC. *Coatings* **2021**, *11* (11), 1298. https://doi.org/10.3390/coatings11111298.
(49) Lin, C.-C.; McCrory, C. C. L. Effect of Chromium Doping on Electrochemical Water Oxidation Activity by $Co_{3-x}Cr_xO_4$ Spinel Catalysts. *ACS Catal.* **2017**, *7* (1), 443–451. https://doi.org/10.1021/acscatal.6b02170.
(50) Wang, W.; Kuai, L.; Cao, W.; Huttula, M.; Ollikkala, S.; Ahopelto, T.; Honkanen, A.-P.; Huotari, S.; Yu, M.; Geng, B. Mass-Production of Mesoporous $MnCo_2O_4$ Spinels with Manganese(IV)- and Cobalt(II)-Rich Surfaces for Superior Bifunctional Oxygen Electrocatalysis. *Angew. Chem. Int. Ed.* **2017**, *56* (47), 14977–14981. https://doi.org/10.1002/anie.201708765.
(51) Zhang, Y.; Zhang, S.; Yuan, M.; Li, Y.; Liu, R.; Nan, C.; Chen, C. Optimal Geometrical Configuration and Oxidation State of Cobalt Cations in Spinel Oxides to Promote the Performance of Li-O_2 Battery. *Nano Res.* **2023**, 17, 221–227. https://doi.org/10.1007/s12274-023-5526-0.
(52) Cai, J.; Zhang, H.; Zhang, L.; Xiong, Y.; Ouyang, T.; Liu, Z. Hetero-Anionic Structure Activated Co-S Bonds Promote Oxygen Electrocatalytic Activity for High-Efficiency Zinc–Air Batteries. *Adv. Mater.* **2023**, *35* (36), 2303488. https://doi.org/10.1002/adma.202303488.
(53) Wang, P.; Ren, Y.; Wang, R.; Zhang, P.; Ding, M.; Li, C.; Zhao, D.; Qian, Z.; Zhang, Z.; Zhang, L.; Yin, L. Atomically Dispersed Cobalt Catalyst Anchored on Nitrogen-Doped Carbon Nanosheets for Lithium-Oxygen Batteries. *Nat. Commun.* **2020**, *11* (1), 1576. https://doi.org/10.1038/s41467-020-

15416-4.
(54) Chen, D.; Lu, R.; Yu, R.; Dai, Y.; Zhao, H.; Wu, D.; Wang, P.; Zhu, J.; Pu, Z.; Chen, L.; Yu, J.; Mu, S. Work-function-induced Interfacial Built-in Electric Fields in Os-$OsSe_2$ Heterostructures for Active Acidic and Alkaline Hydrogen Evolution. *Angew. Chem. Int. Ed.* **2022**. e202208642. https://doi.org/10.1002/anie.202208642.
(55) Sun, J.; Xue, H.; Zhang, Y.; Zhang, X.-L.; Guo, N.; Song, T.; Dong, H.; Kong, Y.; Zhang, J.; Wang, Q. Unraveling the Synergistic Effect of Heteroatomic Substitution and Vacancy Engineering in $CoFe_2O_4$ for Superior Electrocatalysis Performance. *Nano Lett.* **2022**, *22* (8), 3503–3511. https://doi.org/10.1021/acs.nanolett.1c04425.
(56) Zhao, C.; Zhang, X.; Yu, M.; Wang, A.; Wang, L.; Xue, L.; Liu, J.; Yang, Z.; Wang, W. Cooperative Catalysis toward Oxygen Reduction Reaction under Dual Coordination Environments on Intrinsic $AMnO_3$ -Type Perovskites via Regulating Stacking Configurations of Coordination Units. *Adv. Mater.* **2020**, *32* (50), 2006145. https://doi.org/10.1002/adma.202006145.
(57) Liang, J.; Yu, H.; Shi, J.; Li, B.; Wu, L.; Wang, M. Dislocated Bilayer MOF Enables High-Selectivity Photocatalytic Reduction of CO_2 to CO. *Adv. Mater.* **2023**, *35* (10), 2209814. https://doi.org/10.1002/adma.202209814.
(58) Zou, L.; Sa, R.; Zhong, H.; Lv, H.; Wang, X.; Wang, R. Photoelectron Transfer Mediated by the Interfacial Electron Effects for Boosting Visible-Light-Driven CO_2 Reduction. *ACS Catal.* **2022**, *12* (6), 3550–3557. https://doi.org/10.1021/acscatal.1c05449.
(59) Sun, Z.; Zhao, X.; Qiu, W.; Sun, B.; Bai, F.; Liu, J.; Zhang, T. Unlock Restricted Capacity via O-Ce Hybridization for Li-Oxygen Batteries. *Adv. Mater.* **2023**, 35, 2210867. https://doi.org/10.1002/adma.202210867.
(60) Song, Y.; Kong, F.; Sun, X.; Liu, Q.; Li, X.; Ren, L.; Xie, Y.; Shen, Y.; Wang, J. Highly Reversible Solid-State Lithium-Oxygen Batteries by Size-Matching Between Fe-Fe Cluster and $Li_{2-x}O_2$. *Adv. Energy Mater.* **2023**, *13* (4), 2203660. https://doi.org/10.1002/aenm.202203660.
(61) Li, K.; Wang, Z.; Yang, B.; Li, T.; Li, B.; Chen, J.; Yan, Z.; He, M.; Hu, A.; Long, J. Elucidating the Role of Polar Functional Groups in Fluorinated Polymer Artificial Interphase for Stable Lithium Anodes. *Chem. Eng. J.* **2024**, *493*, 152527. https://doi.org/10.1016/j.cej.2024.152527.
(62) He, M.; Shu, C.; Zheng, R.; Li, M.; Ran, Z.; Yan, Y.; Du, D.; Ren, L.; Long, J. Interfacial Interaction between Molybdenum Phosphide and N, P Co-Doped Hollow Carbon Fibers Boosting the Oxygen Electrode Reactions in Zinc-Air Batteries. *Electrochim. Acta* **2021**, *395*, 139211. https://doi.org/10.1016/j.electacta.2021.139211.
(63) Shi, Y.; Zhou, S.; Liu, J.; Zhang, X.; Yin, J.; Zhan, T.; Yang, Y.; Li, G.; Lai, J.; Wang, L. An Integrated Amorphous Cobalt Phosphoselenide Electrocatalyst with High Mass Activity Boosts Alkaline Overall Water Splitting. *Appl. Catal. B Environ.* **2024**, *341*, 123326. https://doi.org/10.1016/j.apcatb.2023.123326.
(64) Shi, Z.; Mao, C.; Zhong, L.; Peng, J.; Liu, M.; Li, H.; Huang, J. Mo-Doped Ni3S4 Nanosheets Grown on Carbonized Wood as Highly Efficient and Durable Electrocatalysts for Water Splitting. *Appl. Catal. B Environ.* **2023**, *339*, 123123. https://doi.org/10.1016/j.apcatb.2023.123123.
(65) Li, R.; Hu, A.; Zhao, C.; Zhou, B.; He, M.; Fan, Y.; Chen, J.; Yan, Z.; Pan, Y.; Long, J. Tailoring Mixed Geometrical Configurations in Amorphous Catalysts to Activate Oxygen Electrode Reactions of Lithium-Oxygen Batteries. *Chem. Eng. J.* **2023**, *452*, 139162. https://doi.org/10.1016/j.cej.2022.139162.
(66) Yan, Y.; Ran, Z.; Zeng, T.; Wen, X.; Xu, H.; Li, R.; Zhao, C.; Shu, C. Interfacial Electron Redistribution of Hydrangea-like NiO@Ni_2 P Heterogeneous Microspheres with Dual-Phase Synergy for High-Performance Lithium–Oxygen Battery. *Small* **2022**, *18* (10), 2106707.

https://doi.org/10.1002/smll.202106707.
(67) Yang, B.; Pan, Y.; Li, T.; Hu, A.; Li, K.; Li, B.; Yang, L.; Long, J. High-Safety Lithium Metal Pouch Cells for Extreme Abuse Conditions by Implementing Flame-Retardant Perfluorinated Gel Polymer Electrolytes. *Energy Storage Mater.* **2024**, *65*, 103124. https://doi.org/10.1016/j.ensm.2023.103124.
(68) Xie, Z.; Lu, Z.; Wang, J.; Qu, Y.; Duan, L. The Surface Electronic Structure Reconstruction of $Co_{2.85}Mn_{0.15}O_4$ with High Active Sites for High-Efficient Lithium–Oxygen Batteries. *ACS Sustainable Chem. Eng.* **2023**, *11* (17), 6698–6709. https://doi.org/10.1021/acssuschemeng.3c00338.
(69) Hu, A.; Chen, W.; Du, X.; Hu, Y.; Lei, T.; Wang, H.; Xue, L.; Li, Y.; Sun, H.; Yan, Y.; Long, J.; Shu, C.; Zhu, J.; Li, B.; Wang, X.; Xiong, J. An Artificial Hybrid Interphase for an Ultrahigh-Rate and Practical Lithium Metal Anode. *Energy Environ. Sci.* **2021**, *14* (7), 4115–4124. https://doi.org/10.1039/D1EE00508A.
(70) He, B.; Li, G.; Li, J.; Wang, J.; Tong, H.; Fan, Y.; Wang, W.; Sun, S.; Dang, F. $MoSe_2$@CNT Core–Shell Nanostructures as Grain Promoters Featuring a Direct Li_2O_2 Formation/Decomposition Catalytic Capability in Lithium-Oxygen Batteries. *Adv. Energy Mater.* **2021**, *11* (18), 2003263. https://doi.org/10.1002/aenm.202003263.

(For Table of Contents Use Only)

Table of Contents (ToC):

$MnCr_{0.5}Co_{1.5}O_4$ efficiently enhances Co^{3+}–O covalency and accelerates charge transfer, thus facilitating the deposition and decomposition of Li_2O_2 in lithium–oxygen batteries.